Asymmetry of parallel flow on the Large Helical Device

Asymmetry of parallel flow on LHD

J. Chen[a], K. Ida[b,c,*], M. Yoshinuma[b,c], T. Kobayashi[b,c], S. Murakami[d], Y. Yamamoto[d], M.Y. Ye[a,*], B. Lyu[e]

[a] *School of Physical Sciences, University of Science and Technology of China, Hefei 230026, China*

[b] *National Institute for Fusion Science, National Institutes of Natural Sciences, Toki, Gifu 509-5292, Japan*

[c] *SOKENDAI (The Graduate University for Advanced Studies), Toki, Gifu 509-5292, Japan*

[d] *Department of Nuclear Engineering, Kyoto University, Kyoto 615-8450, Japan*

[e] *Institute of Plasma Physics, Chinese Academy of Sciences, Hefei 230031, China*

*E-mail: ida@nifs.ac.jp (K. Ida) and yemy@ustc.edu.cn (M.Y. Ye)

Abstract

An asymmetric parallel return flow, which modifies the parallel component of the flow, is expected to meet the zero divergence of the flow on a flux surface based on the common neoclassical theory for torus plasma. Full flow structure is measured by charge exchange spectroscopy on LHD. Inboard/outboard asymmetry of parallel flow is observed according to the full flow profile measurement. Flow asymmetry is considered to be induced by the Pfirsch-Schlüter flow closely associated with the radial electric field. A linear relationship between the integrated flow asymmetry and the electric potential difference is obtained in different magnetic fields and configurations. A model based upon the incompressibility of the flow is applied to acquire a geometric factor *hB*, which only connects to magnetic configuration from experiment. Asymmetric component of parallel flow measured is compared with the asymmetric component of parallel flow calculated in the incompressibility condition of flow on the magnetic flux surface. The measured asymmetric flow is consistent with the calculation in the plasma with small toroidal torque input in the inward shifted configuration. However, the measured asymmetric flow is significantly smaller than that calculated for the plasma with large toroidal torque or in the outward shifted configuration. One possible candidate could be the radial transport due to anomalous perpendicular viscosity plus strongly poloidally asymmetric radial flow.

Keywords: stellarator, flow asymmetry, Pfirsch-Schlüter flow, radial electric field

1. Introduction

Plasma rotation is one of the essential issues since the discovery of the role of $E\times B$ sheared flow in turbulence suppression in H-mode plasma [1, 2] and the clarification of the impact of plasma rotation on MHD instabilities such as resistive wall modes (RWMs) [3, 4]. Plasma rotation is connected to the electric field and ion pressure through the radial force balance. In general, electric potential and ion pressure are constant on a flux surface. Given the toroidal effect, the conservation of poloidal flux causes a difference in poloidal flow between the inboard region and the outboard region. As the standard neoclassical (NC) theory predicts, there is an inboard/outboard asymmetric parallel Pfirsch-Schlüter flow (PS flow) which compensates for the imbalance of perpendicular flux due to the incompressibility of flows ($\nabla\cdot\boldsymbol{v} = 0$) in the steady state [5-7]. This can be understood as a consequence of particle conservation $\nabla\cdot(n\boldsymbol{v}) = 0$ with a constant density on a flux surface and zero first-order radial flow $\boldsymbol{v}\cdot\nabla n = 0$. PS flow represents the return flow of diamagnetic and $E\times B$ flow. Although PS flow is divergence-free on the magnetic flux surface and vanishes after the flux surface average, it redistributes the parallel flow and results in the variation of the parallel flow on a flux surface.

For the axisymmetric system, such as tokamaks, toroidal flow is expected to be dominated by mechanisms except for NC theory because viscosity in toroidal direction vanishes. In stellarators, however, the strong toroidal viscosity damps toroidal flow. Poloidal flow is mainly driven by the radial electric field determined by the ambipolarity condition on the NC radial particle fluxes. Since poloidal flow is coupled to toroidal flow due to the zero divergence of flow (or flow incompressibility), poloidal asymmetry of toroidal flow has been employed to evaluate the poloidal flow on DIII-D [8] and TCV [9], and to calculate the radial electric field on HSX [10, 11]. The poloidal flows are well reproduced by NC theory on DIII-D and TCV, while discrepancies between experimental and predicted radial electric field are observed on HSX, where indications are that radial electric field could be dominated by the non-neoclassical processes for a quasi-symmetric configuration. However, poloidal flows on DIII-D during QH and H mode [12] and on JET with an ITB [13] are not fully understood.

Radial electric field can be modified by changing auxiliary heating and density. In W7-AS, a negative radial electric field in the edge region agrees rather well with the expectations from the ambipolarity condition of NC particle fluxes in neutral beam injection (NBI) L mode discharge [14]. Furthermore, the ‘electron-root’ feature (a positive radial electric field in the core) achieved by electron cyclotron heating (ECH) with central deposition in W7-AS and W7-X shows good agreement with the NC predictions [15, 16]. In addition, on TJ-II, a comparison with NC theory shows quantitative agreement with the measured radial electric field and parallel flow in electron root, and low density plasma without external momentum input [17], while deviations from NC prediction are found for the total incompressible flow in the ion root, and medium density plasma with NBI [18]. In the NBI case, regardless of the fact that asymmetry of the impurity density driven by ion-impurity parallel friction is introduced to explain the observed plasma flows, those modifications due to impurity inhomogeneity are too small to reproduce the compressible flow.

Nevertheless, the particle conservation is usually satisfied and impurities indeed undergo a spontaneous rearrangement on each flux surface at the edge with steep pressure and temperature gradients, making impurity flows compressible [19]. In addition, asymmetry of impurity is present in strongly rotating plasma where the centrifugal force pushes impurities to outside of the torus [20]. On C-Mod [21] and ASDEX Upgrade [22], in order to satisfy the particle conservation equation, the asymmetry of impurity density is postulated to be a factor of 3-6 in the steep gradient region with impurities accumulating in high field side. Recently, in-out asymmetric high-Z impurity accumulation was observed in C-mod. This asymmetry is found to be well described by a combination of centrifugal force, poloidal electric field and the ion-impurity friction effects [23]. Meanwhile, the dependence of compressible flow on the poloidal variation of impurity density is also observed on CHS [24] and ASDEX Upgrade [25], on which the flow structure and impurity asymmetry are in line with NC calculation.

On LHD, plasma flows have been also studied in previous works which focus on the spontaneous flows driven by the radial electric field and ion temperature gradient [26-28]. The measured radial electric fields are found to be in qualitative agreement with those evaluated by NC theory [28-30]. However, toroidal flows show some deviations from NC predictions in the discharges without net external input torque [27, 30]. Evidence shows that the residual stress driven by turbulence can be a candidate for the spontaneous torque [30]. Meanwhile, the flow studies in [30] also suggest that 3D geometry effect on spontaneous flow is of importance in the peripheral region on LHD as well as in the edge of tokamaks when resonant magnetic perturbation (RMP) is applied. In addition, in order to understand the mechanism of spontaneous flows generation, it is also necessary to isolate the terms of driving or damping from those due to 3D geometry configuration.

Full flow structures are well reconstructed by using charge exchange spectrometer (CXS) on LHD. Parallel flow asymmetry, which mainly results from PS flow, is a general phenomenon in NBI and ECH heated discharges. The incompressibility of flows following the usual NC is applied to data analysis in order to perform a comparison with NC prediction.

2. Experimental setup

LHD is a device of the heliotron configuration with toroidal and poloidal periods of N=10 and M=2, respectively. Three tangential NBIs (NB1, NB2 and NB3) with negative ion source and the total power of 16 MW and two perpendicular NBIs (NB4 and NB5) with

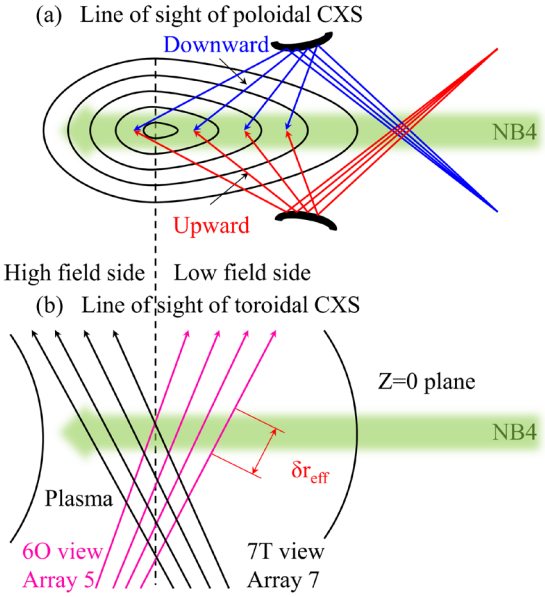

Figure 1. Schematics of charge exchange spectroscopy on LHD for (a) poloidal CXS viewed from poloidal cross section and (b) toroidal CXS viewed from z = 0 horizontal plane.

positive ion source and the power of 12 MW have been installed [31]. The injection direction of NB1 is the same as that of NB3, but is opposite to that of NB2. On LHD, as shown in Figure 1, four sets of CXS arrays, which collect the light emitted from the plasma during charge exchange interactions between carbon impurities and the same perpendicular NBI (NB4) atoms, are applied to measure the toroidal and poloidal flow velocity [32].

For the poloidal flow measurement, as shown in Figure 1 (a), there are two 24 channel viewing array. One array is viewing upward and the other is viewing downward. This bi-direction viewing array is employed to eliminate the effect of energy dependency cross section on flow measurement [33]. The distance between two observation radii of poloidal CXS changes from 33cm for the channel farthest inside to 1.3cm for the channel farthest outside. In order to acquire the full profile of toroidal flow, radii of two sets of toroidal CXS with 19 channels for the high field side (HFS) and 35 channels for LFS shown in Figure 1 (b) are arranged along the path of NB4 and three observation radii of these channels cross around the magnetic axis. According to the relationship between the ratio of the correction velocity to ion temperature and beam energy from poloidal CXS, the measured toroidal flow velocity is also corrected by the additional velocity due to the energy dependence cross section.

3. Flow on the flux surface

In general, particles are always conserved in steady state, which means that particle flux is zero divergence or satisfies the continuity equation. Hence flow becomes incompressible when the radial flow is negligible and density is the function of the flux surface. PS flow originates from the incompressibility of the flow. Foundational equations describing PS flow have been presented in previous papers [10, 11, 34] and are applied to analyze the experimental data.

The incompressibility of ion flow leads to the condition that

$$\nabla\cdot(\boldsymbol{v}_{i\perp}+\boldsymbol{v}_{i\parallel})=0 \tag{1}$$

where $\boldsymbol{v}_{i\perp}$ and $\boldsymbol{v}_{i\parallel}$ are the ion flow velocity perpendicular and parallel to the magnetic field line, respectively. It should be pointed out that the radial flow velocity is ignored in equation (1) because it is almost zero in plasma. The perpendicular flow is given by the radial force balance,

$$\boldsymbol{v}_{i\perp}=\frac{\boldsymbol{E}\times\boldsymbol{B}}{\boldsymbol{B}^2}-\frac{\nabla P_i\times\boldsymbol{B}}{Z_i e n_i \boldsymbol{B}^2}=-\left(\frac{\mathrm{d}\phi}{\mathrm{d}\psi}+\frac{1}{Z_i e n_i}\frac{\mathrm{d}P_i}{\mathrm{d}\psi}\right)\frac{\nabla\psi\times\boldsymbol{B}}{B^2} \tag{2}$$

where $\boldsymbol{E}$ is the electric field, $\boldsymbol{B}$ magnetic field, P_i ion pressure, Z_i the charge, e elementary charge, n_i ion density, ϕ electric potential, and ψ flux surface. Although P_i, n_i, and ϕ are usually the function of the flux surface, poloidal flow, which is mainly determined by $\boldsymbol{E}\times\boldsymbol{B}$ term (or $\boldsymbol{v}_{i\perp}$), has a strong asymmetry structure because of the variation of the radial electric field, $E_r = -(\mathrm{d}\phi/\mathrm{d}\psi)/(\mathrm{d}\psi/\mathrm{d}r)$, on a flux surface. The asymmetry leads to the non-zero divergence of the perpendicular flow, which is compensated for by the PS flow from the parallel flow to satisfy the flow incompressibility condition. Therefore, parallel flow can be written as two terms, divergence free flow and PS flow,

$$\boldsymbol{v}_{i\parallel}=\boldsymbol{v}_{\mathrm{sym}}+\boldsymbol{v}_{\mathrm{asym}} \tag{3}$$

where the symmetric flow $\boldsymbol{v}_{\mathrm{sym}}$ is the zero divergence on a flux surface and asymmetric flow $\boldsymbol{v}_{\mathrm{asym}}$ varies on a flux surface with the average over flux surface zero.

Using equation (1), (2) and (3), asymmetric flow can be expressed as,

$$\boldsymbol{v}_{\mathrm{asym}}=\left(\frac{\mathrm{d}\phi}{\mathrm{d}\psi}+\frac{1}{Z_i e n_i}\frac{\mathrm{d}P_i}{\mathrm{d}\psi}\right)h\boldsymbol{B} \tag{4}$$

where h is a geometrical factor defined by

$$\boldsymbol{B}\cdot\nabla h=-2\frac{(\boldsymbol{B}\times\nabla B)\cdot\nabla\psi}{B^3}, \tag{5}$$

$$\left\langle hB^2\right\rangle=0. \tag{6}$$

Usually, $1/h$, which depends only on the magnetic configuration, represents how much the generic field changes along the magnetic field. h can be solved in Boozer coordinates [35] by using the Fourier series in poloidal (θ) and toroidal angles (ζ) with poloidal (m) and toroidal (n) mode numbers of the spectral component of the magnetic field [36, 37]. Then h can be expressed as

$$h=\frac{1}{B_0^2}\sum_{m,n}\frac{nI+mG}{n-\iota m}\delta_{m,n}\cos(n\zeta-m\theta), \tag{7}$$

where ι, I and G are, respectively, the rotational transform, the toroidal current enclosed within a flux surface and the total poloidal current external to a flux surface. $\delta_{m,n}$ is the coefficient of the Fourier expansion of $1/B^2$ along a field line. Figure 2 shows one example of the radial profile of the magnetic spectrum on LHD, where the toroidal components are deduced from the natural periodicity of LHD, n' = n/N. It can be seen that the dominant components are the modes (n, m) of (0, 1), (10, 1), (10, 2), (10, 3) and (-10, 0). The mode (-10, 0) is large in the core but small in the edge, which is opposite to the performance

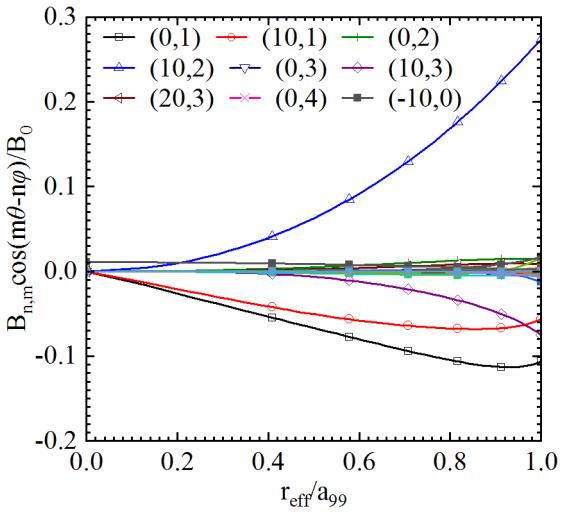

Figure 2. Radial profile of the magnetic spectrum in LHD for the vacuum magnetic axis of 3.60m.

of other dominant modes. The existence of asymmetric flow redistributes the parallel flow on a flux surface and can result in asymmetry of parallel flow as long as the radial electric field and ion pressure gradient appear.

4. Experimental results

CXS on LHD can provide a full profile of the toroidal flow and a half profile of the poloidal flow on LFS. The parallel and perpendicular flows are acquired from the measured flow by considering the angles between toroidal flow and poloidal flow and magnetic field lines. The explicit relation can be written as

$$v_{i\parallel} = (v_{\mathrm{tor}}B_{\varphi} - v_{\mathrm{pol}}B_{\theta})/B, \quad (8)$$

$$v_{i\perp} = (v_{\mathrm{tor}}B_{\theta} + v_{\mathrm{pol}}B_{\varphi})/B, \quad (9)$$

where v_{tor} is toroidal flow velocity, v_{pol} poloidal flow velocity, B_{φ} magnetic field in toroidal direction and B_{θ} magnetic field in the poloidal direction. The sign of poloidal flow is defined as positive for ion diamagnetic and negative for electron diamagnetic direction.

Two assumptions are made in order to obtain the full flow structure because of the lack of poloidal flow measurement in HFS. First, ϕ, P_i, and n_i are functions of ψ. Second, the inverted poloidal flow is used to eliminate the integration effect on the flow structure. E_r in LFS is calculated through the radial force balance equation (2),

$$E_{r,\mathrm{LFS}} = \frac{\nabla P_{i,\mathrm{LFS}}}{Z_i e n_{i,\mathrm{LFS}}} + v_{\mathrm{tor,LFS}}B_{\theta,\mathrm{LFS}} + v_{\mathrm{pol,LFS}}B_{\varphi,\mathrm{LFS}}, \quad (10)$$

where the subscript of LFS means that the parameters are in LFS. Then, ϕ in LFS is expressed as

$$\phi_{\mathrm{LFS}} = \int_0^{R_{\mathrm{edge}}} E_{r,\mathrm{LFS}}\mathrm{d}R_{\mathrm{LFS}}, \quad (11)$$

where R_{LFS} and R_{edge} are the observation major radius in LFS and the farthest outside major radius in LFS, respectively. Given that the observation radii in HFS are not exactly equal to those in LFS, interpolation using ϕ_{LFS} is used to obtain electric potential in HFS ϕ_{HFS} with constant ϕ on a flux surface. As a result, E_r in HFS is

$$E_{r,\mathrm{HFS}} = \mathrm{d}\phi_{\mathrm{HFS}} / \mathrm{d}R_{\mathrm{HFS}}, \quad (12)$$

where R_{HFS} is the major radius in HFS. According to equation (10), the poloidal flow in HFS can be written as

$$v_{\mathrm{pol,HFS}} = (E_{r,\mathrm{HFS}} - \frac{\nabla P_{i,\mathrm{HFS}}}{Z_i e n_{i,\mathrm{HFS}}} - v_{\mathrm{tor,HFS}}B_{\theta,\mathrm{HFS}}) / B_{\varphi,\mathrm{HFS}}, \quad (13)$$

where the subscript of HFS means that the parameters are in HFS. It should be mentioned that P_i and n_i in equation (13) are considered to be the same as those in LFS based on the first assumption. Therefore, parallel and perpendicular flows are obtained by applying equations (8) and (9). Then, the symmetric flow is the averaged flow of measured parallel flows in LFS and HFS because it is a flux function. Asymmetric flow is the difference of parallel and symmetric flows. Since symmetric flow, ϕ and P_i have been obtained from experiments, these quantities can be used to verify the consistency of the factor hB which appears in NC theory, see equation (4). In order to distinguish the measured asymmetric coefficient from the equilibrium hB calculated from equation (5) and (6), the measured asymmetric coefficient C_{asym} is defined as the ratio of measured asymmetric parallel flow to the sum of the pressure and electric potential gradient terms,

$$C_{\mathrm{asym}} = \boldsymbol{v}_{\mathrm{asym}} / (\frac{\mathrm{d}\phi}{\mathrm{d}\psi} + \frac{1}{Z_i e n_i}\frac{\mathrm{d}P_i}{\mathrm{d}\psi}). \quad (14)$$

It should be noted that the spatial resolution of poloidal CXS is degraded in the core region by the integration effect due to the long cross path between line of sight and NBI, which is defined as the effective intersection δr_{eff} shown in Figure 1 (b). Figure 3 shows the effect of the integration on flow velocity and the radial electric field. It can be observed in Figure 3(a) that the integration effect is larger in the core and smaller in the edge. The angle between line of sight and NB4 increases gradually up to 90° as the observation radius moves outward, which results in the reduction of the effective flux surface region that the line of sight crosses. As a consequence, as shown in Figure 3(b), the real poloidal flow in the core is smoothed much more strongly by the integration effect than that in the edge, especially in the region with peaked flow profile where the difference can reach to approximately 30%. However, measured poloidal flow is almost the same as the inverted poloidal flow in the outer region with small cross path. The fitted and inverted poloidal flows are obtained by using cubic spline function with the condition that poloidal flow velocity is zero at the core. The fitted poloidal flow is directly calculated from original data by the least square curve fitting. The inverted poloidal flow is acquired in another indirect way. First, an inverted poloidal flow satisfying formerly mentioned function is assumed. Then, integration along the cross path at each observation radius is made by using assumed poloidal flow to calculate the integrated flow. Finally, the integrated profile including the integration effect is utilized to fit with original data in order to obtain the inverted poloidal flow.

The radial electric field calculated according to the radial force balance is shown in Figure 3(d). The radial electric field shows the same tendency with poloidal flow

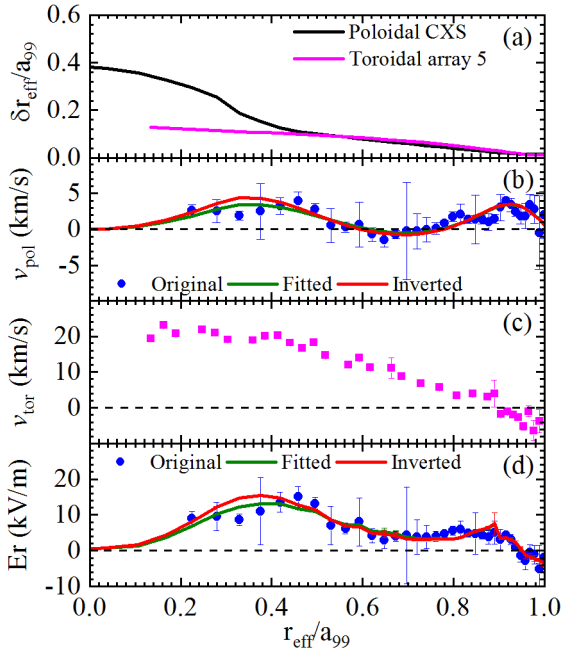

Figure 3. Integration effect of CXS (SN133508) on LHD (a) effective intersection for poloidal CXS (black) and toroidal array 5 (magenta), (b) measured (blue circle), fitted (olive line) and inverted (red line) poloidal flow velocity, (c) toroidal flow velocity measured by toroidal array 5 and (d) measured (blue circle), fitted (olive line) and inverted (red line) radial electric field.

but with a smaller difference of approximately 20%. It should be mentioned that the integration effect for toroidal CXS on LHD shown in Figure 3(a) is relatively smaller with $\delta r_{eff}/a_{99}$ less than 0.1 because each line of sight of toroidal CXS is closely located at the region parallel to the flux surface. Hence, measured toroidal flow in Figure 3(c) is utilized to calculate the radial electric field. Although the influence on the radial electric field becomes smaller due to the ignorable integration effect on toroidal flow, the difference between the measured and inverted poloidal flows and radial electric fields cannot be neglected. Therefore, it is necessary to consider the integration effect to acquire the actual flow structure.

Figure 4 shows the time traces of the flow structure in two density decay discharges, with one discharge decreasing from $2.0\times10^{19}m^{-3}$ to $0.9\times10^{19}m^{-3}$ (Figure 4 (c)) and another from $2.1\times10^{19}m^{-3}$ to $1.7\times10^{19}m^{-3}$ (Figure 4 (d)). As shown in Figure 4(a), the heating power of tangential NBI P_{tan}, is 8.7MW and that of perpendicular NBI, P_{perp} is 9.0MW for SN133708. As shown in Figure 4(b), the heating power of P_{tan} is 1.6MW and that of P_{perp} is 13MW for SN138706. As shown in Figure 4(e) and (f), ion temperatures for both cases are almost symmetric in HFS ($r_{eff}/a_{99}<0$) and LFS ($r_{eff}/a_{99}>0$). Ion temperature for SN133708 is much higher than that for SN138706 due to the higher NBI powers. Parallel flow for SN133708 in Figure 4(g) shows a strong asymmetry with flow negative in HFS and flow positive in LFS. In addition, strength of asymmetry of parallel flow (asymmetric flow), as shown in Figure 4(k), increases with density decreasing in decay phase and reaches a steady level in steady density phase. It seems that electron density is the key which affects the asymmetry of parallel flow. However, flow structure for SN138706 overthrows this prediction. On one hand, parallel flow shown in Figure 4(h) presents a steady peaked profile despite of the density decrease. Meanwhile, asymmetric flow shown in Figure 4(l) almost stays unchanged during the reduction in density as well. The steady parallel and symmetric flow is due to the small change of the electron density. On the other hand, parallel flow in LFS is slightly lower than that in HFS and asymmetric flow reverses with positive in HFS and negative in LFS, which is opposite to the situation of SN133708. Therefore, what affects asymmetric flow is not directly associated with electron density.

Figure 4(i)(j) show the perpendicular flow. Weak asymmetry is also seen in perpendicular flow and the magnitude of the perpendicular flow in LFS is slightly larger than that in HFS in both cases. In order to satisfy the continuity condition, the non-zero divergence of the perpendicular flow is compensated for by the asymmetric flow in the parallel direction. In addition, it is clear that perpendicular flow is in the ion diamagnetic direction for SN133708 but changes to electron diamagnetic direction for SN138706. The radial electric field determined mainly by the perpendicular flow term shows the same tendency of the perpendicular flow and is reversed in two cases. The radial electric field is positive for SN133708 as shown in Figure 4(m) and negative for SN138706 as shown in Figure 4(n), which corresponds to the reversal of the direction of asymmetric parallel flow. Meanwhile, the strength of the radial electric field also remains consistent with that of asymmetric flow. Therefore, it can be concluded that the asymmetric flow depends mainly on the radial electric field. It should be mentioned that the sign of the radial electric field can be controlled by changing the collisionality [29, 38]. The transition of the radial electric field from a negative to a positive value (i.e. from ion to electron root, which is the concept first proposed in [39]) can happen when the collision frequency is low enough. As shown in Figure 4(c)(d), the electron density for SN133708 is lower than that for SN138706, while the temperature for the former is higher than that for the latter. Since the collisionality decreases with the decreasing electron density and increasing temperature, the collisionality for SN133708 is much lower than that for SN138706, which could result in the reversal of the radial electric field. The asymmetric coefficient C_{asym} shown in Figure 4(o)(p) almost stays constant even though asymmetric flow varies with time. Scatters of C_{asym} for density decay before 4.7s are caused by the small radial electric field.

Figure 5 shows the profiles of the flow at two time slices indicated by the dash line in Figure 4. It is seen much more clearly that the radial electric field shown in Figure 5(i)(j) changes sign because of the different directions of perpendicular flow shown in Figure 5(c)(d) for both cases, which results in the reversal of asymmetric flow shown in Figure 5(e)(f). It should be noticed in Figure 5(i)(j) that the radial electric field is not symmetric in HFS and LFS because the distance between two neighboring flux surfaces is different at the two sides. In

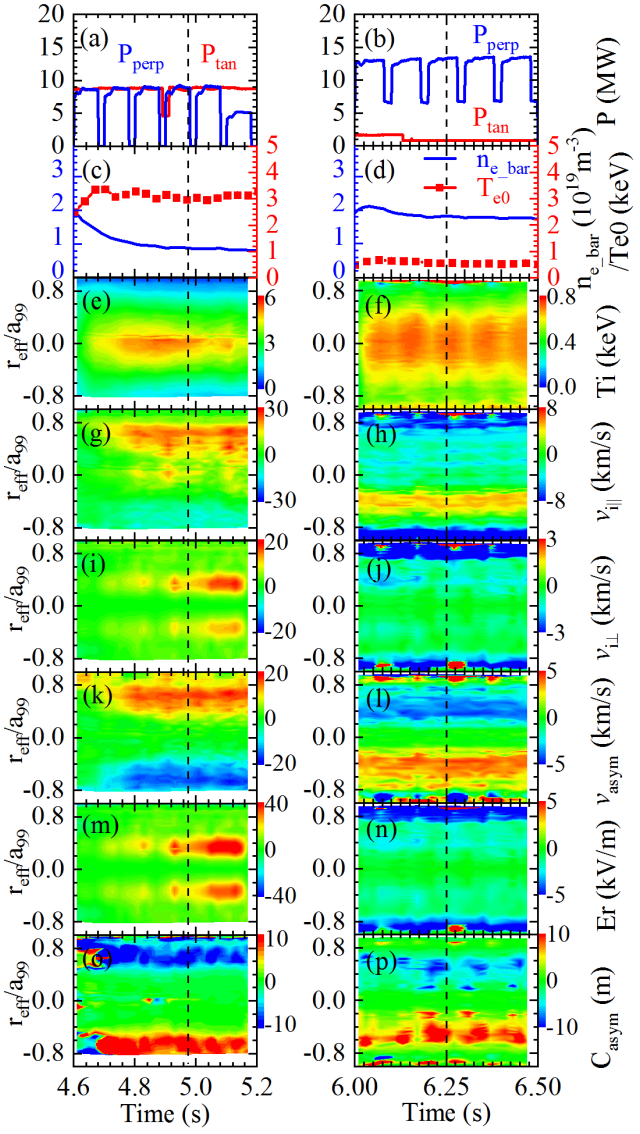

Figure 4. Two-dimensional structures of plasma flow in density scan discharge with positive (SN133708) and negative (SN138706) radial electric field. Panels from top to bottom are (a)(b) tangential (red) and perpendicular (blue) NBI heating power, (c)(d) line averaged electron density (blue line) and electron temperature (red line with square) in the core, (e)(f) ion temperature, (g)(h) parallel flow velocity, (i)(j) perpendicular flow velocity, (k)(l) asymmetric flow, (m)(n) radial electric field, and (o)(p) coefficient of the asymmetric parallel flow measured from experiment. The magnetic configurations for SN133708 and SN138706 are (R_{ax}, B_t, gama, B_q) of (3.60, -2.85, 1.2538, 100) and (3.90, -1.375, 1.2538, 100), respectively. R_{ax}, B_t, gama, and B_q the vacuum magnetic axis, toroidal magnetic field strength, pitch parameter, and quadruple field, respectively. The dash lines indicate the time slice for profiles shown in Figure 5.

contrast, electric potential shown in Figure 5(g)(h) is symmetric. The denser the flux surface is, the larger the radial electric field becomes. In addition, C_{asym} shown in Figure 5(k)(l) is anti-symmetric in HFS and LFS because of the assumption that ϕ, P_i, and n_i are the function of the flux surface. In fact, the equilibrium hB is a geometric factor based on the magnetic configuration and can be distorted from the anti-symmetric structure when magnetic configuration changes. Therefore, there would be a difference between C_{asym} and the equilibrium hB.

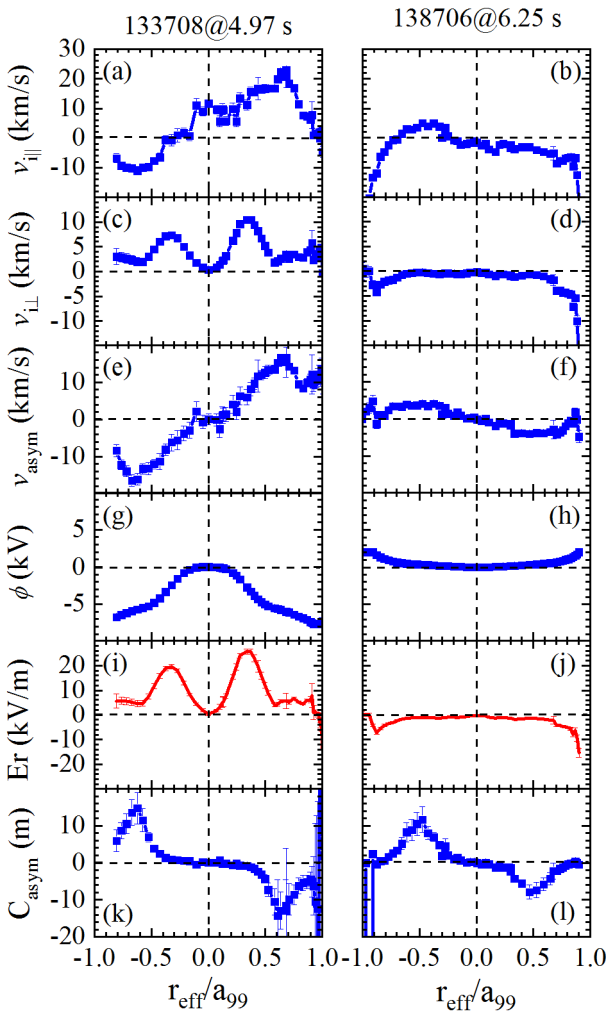

Figure 5. Profiles of plasma flow in density scan discharge with positive radial electric field (SN133708 at 4.97s) and with negative radial electric field (SN138706 at 8.04s). Panels from top to bottom are (a)(b) parallel flow velocity, (c)(d) perpendicular flow velocity, (e)(f) asymmetric flow, (g)(h) electric potential, (i)(j) radial electric field and (k)(l) coefficient of the asymmetric parallel flow measured from experiment.

Another discharge with modulated ECH as shown in Figure 6 shows clearer evidence for the relationship between asymmetric flow and the radial electric field. The modulation frequency of ECH is 2.5Hz and the density increases from 0.8×10^{19}m^{-3} to 1.1×10^{19}m^{-3}. It can be seen in Figure 6(d) that the parallel flow is positive and shows strong asymmetry during ECH phase and that the parallel flow is almost static without ECH. As shown in Figure 6(f), asymmetric flow calculated from parallel flow also responds to ECH modulation. The asymmetry is strong in ECH phase and almost zero without ECH. The change of the measured asymmetric parallel flow with ECH is due to the enhanced $E\times B$ drift driven by ECH. Although the strength of asymmetric flow decreases with the increasing electron density slightly, asymmetric flow shows the same tendency of the radial electric field shown in Figure 6(g). Asymmetric flow becomes strong with large radial electric field and almost disappears with a small radial electric field. Electron density is merely an indirect way to influence the radial electric field. Figure 7 is the

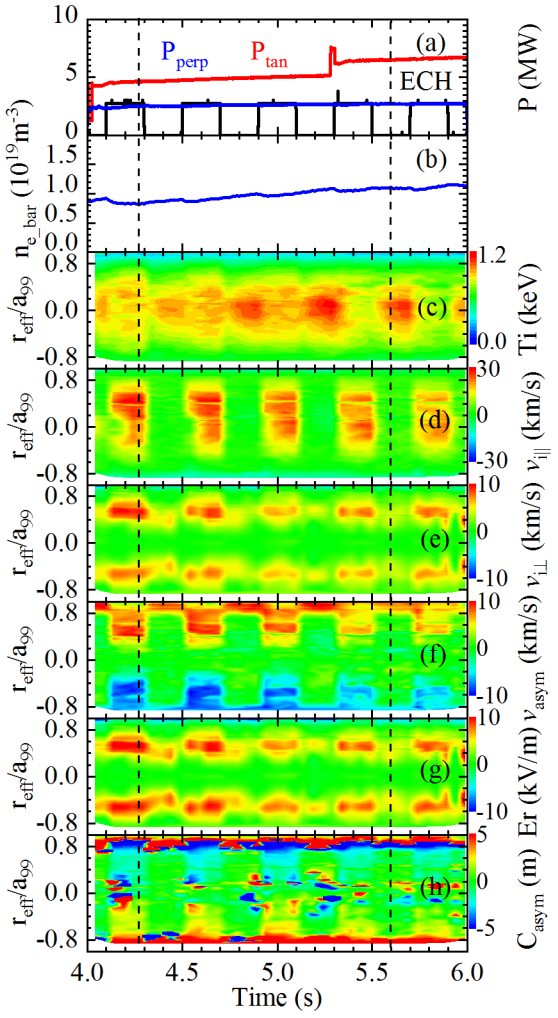

Figure 6. Two-dimensional structure of plasma flow in modulated ECH (SN129966). Panels from top to bottom are (a) tangential (red) and perpendicular (blue) NBI and ECH (black) heating power, (b) line averaged electron density in the core, (c) ion temperature, (d) parallel flow velocity, (e) perpendicular flow velocity, (f) asymmetric flow, (g) radial electric field and (h) coefficient of the asymmetric parallel flow measured from experiment. The magnetic configuration for SN129966 is (R_{ax}, B_t, gama, B_q) of (3.60, -1.375, 1.2538, 100). The dash lines represent the time slices for profiles shown in Figure 7.

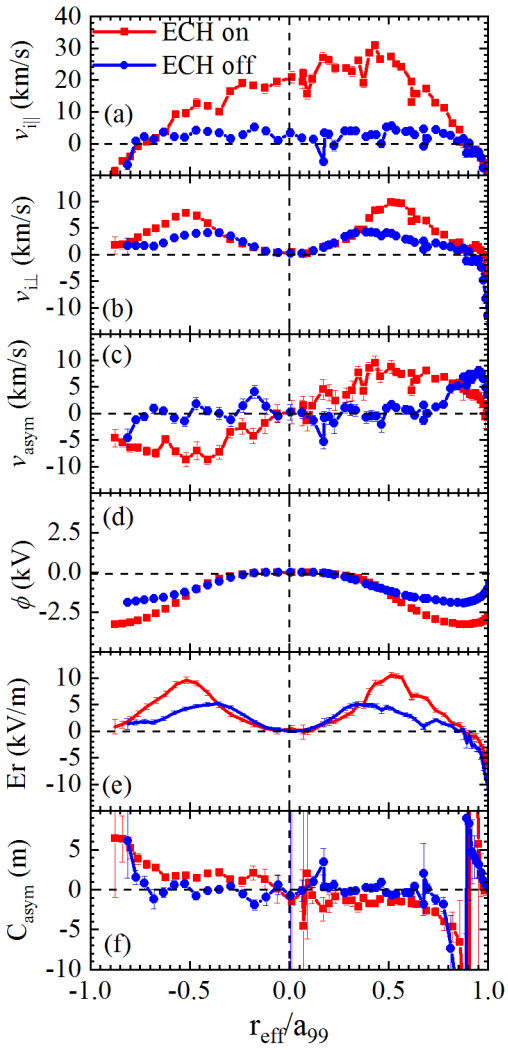

Figure 7. Profile of plasma flow in modulated ECH (SN129966) at 4.29s (ECH on, red square) and 5.59s (ECH off, blue circle). Panels from top to bottom are (a) parallel flow velocity, (b) perpendicular flow velocity, (c) asymmetric flow, (d) electric potential, (e) radial electric field and (f) coefficient of the asymmetric parallel flow measured from experiment.

comparison between the profiles of the flow with ECH and those without ECH. It can be seen from Figure 7(a) that parallel flow profile is flat in the absence of ECH and becomes positive with ECH on. Further, the increase of parallel flow in LFS is larger than that in HFS. The change of parallel flow results from two contributions. First, ECH drives parallel flow to increase in co-direction. Second, the induced flow is redistributed by the appearance of the asymmetric flow on a flux surface. It should be noticed in Figure 7(c)(e) that there is almost no asymmetric flow even with a finite radial electric field when ECH is off. There seem to be some offset of the radial electric field. This offset may result from the scattering of the scaling of the experimental data shown in the next section.

To achieve better understanding of the relationship between asymmetric flow and radial electric field, one global comparison is applied. Asymmetric flow is integrated from HFS to LFS along ψ, which is expressed as $\pi B r_{eff}^2$. And the integration of the radial electric field is twice the difference of the electric potential in the core and of that in the edge. Figure 8 shows the relationship between integrated asymmetric flow and electric potential with different magnetic fields (1.375T, 2.75T and 2.85T) in the same magnetic configuration of the magnetic axis (R_{ax}) of 3.6m. Although there are more experimental data scattered in the correlation, it can be observed that the integrated asymmetric flow increases linearly with the electric potential. In addition, integrated asymmetric flow becomes negative in negative electric potential difference, which means that asymmetric flow reverses when the direction of radial electric field changes. It should be pointed out that the data shown in Figure 8 come from a sequence of discharges nearby with the same magnetic field and that one point denotes a time slice. In addition, for the same magnetic configuration, the linearity between the integrated asymmetric flow and the electric potential difference are nearly the same in different magnetic fields.

The slope shown in Figure 8 which represents the impact of the radial electric field on asymmetric flow is approximately 3.4 m.

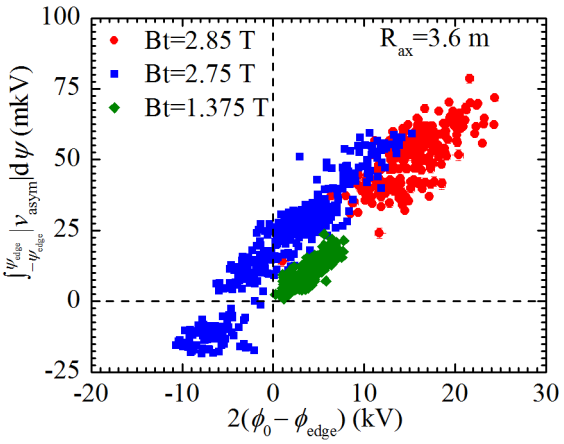

Figure 8. Relationship between integrated asymmetric flow and electric potential with different magnetic fields in the same magnetic axis of 3.6 m. The magnetic fields are 1.375 T (olive diamond), 2.75T (blue square) and 2.85 T (red circle).

5. Comparison of experiments with neoclassical theory

Two typical discharges, one with large symmetric flow gradient and the other with a small gradient in the same magnetic configuration, are used to make a comparison with calculation in order to validate the measured asymmetric coefficient C_{asym}. The large gradient flow is induced by two co-direction tangential NBI heating together with one perpendicular NBI modulation for diagnostic. As shown in Figure 9(a), symmetric flow profile is peaked with a large gradient and redistributed by asymmetric flow with a decrease in HFS and increase in LFS. It can be seen from Figure 9(e) that C_{asym} shows good agreement with calculation in the outer region ($|r_{eff}/a_{99}| > 0.5$) where the flow gradient is relatively small. However, difference between experiment and calculation is observed in the inner region ($|r_{eff}/a_{99}| < 0.5$) where the flow gradient is large. Since C_{asym} is obtained according to equation (14) based on the incompressibility of the flow, the distinction between experiment and calculation indicates that the flow is compressible in the inner region. As shown in Figure 9(c), radial electric field reaches the peak at $|r_{eff}/a_{99}| \sim 0.35$ and is large in the core while asymmetric flow is almost zero, which leads to the discrepancy with calculation. For the case of small flow gradient, there is no net torque input and the flow is driven by pure ECH and perpendicular NBI blips for diagnostic. As shown in Figure 9(b), plasma flows in the direction parallel to magnetic field in LFS and reverses in HFS because of the existence of asymmetric flow. Combined with Figure 9(d), asymmetric flow and radial electric field almost peak at the same position of $|r_{eff}/a_{99}| \sim 0.4$. It can be seen in Figure 9(f) that C_{asym} is consistent with the calculation in the region ($|r_{eff}/a_{99}| < 0.9$) with small flow gradient though scatter of C_{asym} appears in edge because of zero radial electric field, which is also observed in the peaks flow profile case.

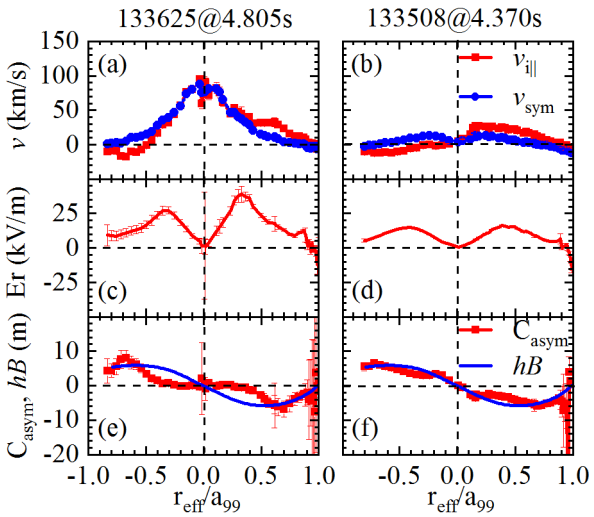

Figure 9. Measured coefficient of the asymmetric parallel flow in comparison with the equilibrium *hB* in the discharge with large (SN133625) and small (SN133508) gradient of symmetric flow. (a)(b) parallel (red square) and symmetric flow (blue circle), (c)(d) inverted radial electric field and (e)(f) measured asymmetric coefficient from experiment (red square) and the equilibrium (blue line) *hB*. The magnetic configurations for SN133625 and SN133508 are (R_{ax}, B_t, gama, B_q) of (3.60, -2.85, 1.2538, 100) and (3.60, -2.75, 1.2538, 100), respectively.

Since *hB* is a factor depending only on the magnetic configuration, as shown in Figure 9(e)(f), the equilibrium *hB* for the same magnetic configuration is similar to each other not only in profile but also in magnitude. Therefore, it is necessary to perform some comparison between experiment and calculation in different magnetic configurations in order to investigate the availability of incompressibility of the flow.

On LHD, magnetic configuration can be modified by the shift of the R_{ax} from 3.50m to 4.00m. Magnetic field configurations with R_{ax} equal to 3.55m, 3.60m, 3.75m and 3.90m are used to investigate the influence of magnetic configuration on asymmetric flow. The sets of discharges with R_{ax} = 3.55m, 3.75m and 3.90m are heated by balanced NBI with ECH, tangential NBI with modulated ECH, and perpendicular NBI, respectively. Figure 10 represents each magnetic configuration. Figure 10(a)(b)(c) shows the measured and calculated asymmetric flow, where the calculated asymmetric flow is obtained by using the equilibrium *hB* according to equation (4). The measured asymmetric flow shows quantitative agreement the calculated flow for R_{ax} of 3.55m. Nevertheless, disagreement is observed for R_{ax} of 3.75m and 3.90m, especially in LFS. For R_{ax} of 3.55m, C_{asym} is consistent with the equilibrium *hB* when there is no net torque input. However, discrepancy is shown for R_{ax} of 3.75m and 3.90m. Besides, as shown in Figure 9(e)(f) and Figure 10(g)(h)(i), the equilibrium *hB* increases with the increasing magnetic axis from 3.55m to 3.90m, which means that the *hB* factor is higher in outward shifted magnetic axis. Figure 10 (j)(k)(l) show the anomalous flow which is defined as the difference between the measured and the calculated asymmetric flow. It can be observed that the anomalous asymmetric flow is smallest for R_{ax} of 3.90m and the strength of anomalous flow for

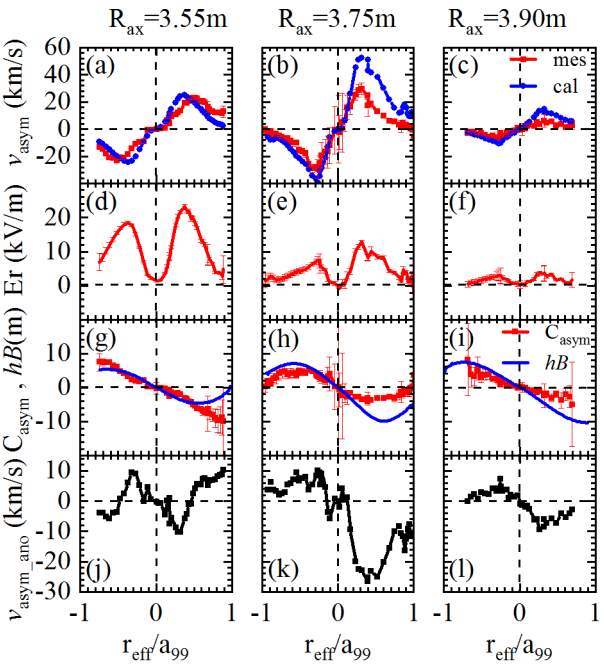

Figure 10. Measured coefficient of the asymmetric parallel flow in comparison with the equilibrium *hB* in different magnetic configurarions. (a)(b)(c) measured (red square) and calculated asymmetric flow (blue circle), (d)(e)(f) the inverted radial electric field, (g)(h)(i) the measured asymmetric coefficient (red square) and the equilibrium (blue line) *hB*, and (j)(k)(l) the anomalous asymmetric parallel flow which represents the difference between the measured and calculated asymmetric parallel flow. (a)(d)(g)(j), (b)(e)(h)(k) and (c)(f)(i)(l) are for magnetic axis of 3.55m, 3.75m and 3.90m, respectively.

R_{ax} of 3.55m is comparable to that for R_{ax} of 3.75m. This is because the anomalous flow is proportional to the radial electric field. After the impact of the radial electric field on anomalous flow is eliminated, the tendency will be consistent with what is observed in Figure 10(g)(h)(i).

Figure 11 shows the statistic for different magnetic configurations. It should be mentioned that the calculated lines are based on the flux averaged equilibrium *hB* according to the calculation from equation (5) and (6). As shown in Figure 11(a), for R_{ax} of 3.55m, the calculation well predicts the experimental results without torque input when the electric potential difference is less than 10 kV. However, the calculation underestimates the asymmetric flow with high electric potential difference even though external torque is not input. The relationship between integrated asymmetric flow and electric potential distorts away from linearity. For R_{ax} of 3.60m, as shown in Figure 11 (b), the statistic with ECH and that with NBI are the discharges in the neighboring shots of SN133508 and those in the neighboring shots of SN133625, respectively. The tendency for discharges with only ECH is similar to non-linearity of R_{ax} of 3.55m. When the electric potential difference is small, the predicted asymmetric flow is larger than the experimental flow. The discrepancy increases together with the electric potential difference. Asymmetric flow of SN133508 is located in the cross of calculation and experiments. For R_{ax} of 3.60m with NBI, the asymmetric flow is always overestimated by the calculation though integrated asymmetric flows are linear with electric potential difference. For Rax = 3.75m and

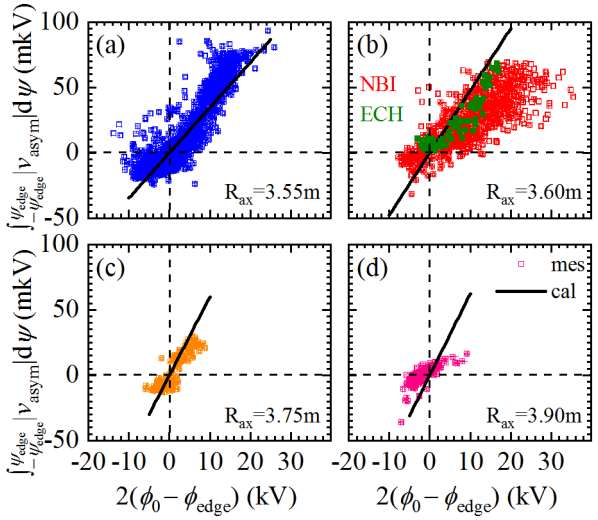

Figure 11. Relationship between integrated asymmetric flow and electric potential for magnetic axis of (a) 3.55m, (b) 3.60m, (c) 3.75 m and (d) 3.90m. For magnetic axis of 3.60m, the data with external torque input (red) and those without external torque (olive green) are plotted together.

3.90m, as shown in Figure 11(c)(d), there remains overestimation even without external torque input when the electric potential difference is small.

6. Discussion and summary

Incompressibility of flows is an approximation of the particle conservation in a steady state with constant impurity density on a flux surface and radial flow eliminated. In fact, impurity density is linked to flow due to the zero divergence of particle flux. As a result, flow becomes compressible in the presence of asymmetric impurity density and poloidal redistribution of impurity density on a flux surface in turn modifies the flow structure. Therefore, one possible explanation of the discrepancy between the measured C_{asym} and equilibrium *hB* is the variation of impurity in poloidal direction.

Models which consider the impact of impurity density asymmetry on flow structure have been applied to infer the required impurity density asymmetry [21, 22]. Deduction that impurity density in HFS is larger than that in LFS with a factor of 3-6 is expected. For the case with larger flow gradient, the equilibrium *hB* is much larger than C_{asym} in the core. Thus, calculated asymmetric flow according to equation (4) originating from flow incompressibility will be larger than the experimental asymmetric flow as well. In order to remain consistent with experiments, the calculated symmetric flow should be reduced to a lower level, which means that poloidal variations of poloidal flow should be partly compensated for by the inhomogeneity of impurity density on a flux surface. Therefore, accumulation of impurity density in HFS is necessary for the reduction of asymmetric flow. However, this postulation is not confirmed by carbon density from experiment. The carbon density accumulates more in LFS in this case. This discrepancy shown in the larger flow gradient case indicates that impurity density asymmetry is not appropriate enough to explain the asymmetry of

parallel flow though impurity density asymmetry indeed modifies flow structure on a flux surface.

In the assumption of flow incompressibility, the radial flow is also ignored in the usual NC theory. Radial transport could make an impact on the flow structure on a flux surface by carrying particles or momentum from one flux surface to the location of interest when radial transport is comparable to the parallel transport. The radial flux is proportional to the velocity gradient with the expression of $\mu_\perp \nabla v_{i//}$, where $\mu_\perp$ is the perpendicular viscosity coefficient.

The change of the radial transport can result from two reasons, flow gradient and $\mu_\perp$. On one hand, the diffusion of parallel flow along radial direction becomes larger when peaked parallel flow profile driven by strong torque from NBI appears, which may be an explanation for the disagreement for large flow gradient in Figure 9(c) though the magnetic configuration is the same in both cases. On the other hand, augmentation of $\mu_\perp$ may also lead to the increase of radial transport even with a small flow gradient. In such cases, NC theory is not appropriate to describe the flow structure. On LHD, an enhancement of the confinement has been observed in the inward shifted magnetic axis [40], which is an indirect indication that the radial transport becomes larger for outward shifted magnetic axis. In addition, in the edge region of LHD there is a stochastic layer whose width increases with the value of R_{ax} [41]. The flattening of the electron temperature and that of the delay time of the heat pulse have been observed in the edge [42]. The importance of the magnetic stochasticity has been extensively studied in the RFX-mod reversed field pinch, where huge flow modifications in the edge plasma follows the transition from a magnetic topology with a (m, n) = (1, 7) helical order to chaos [43, 44]. Besides, the impact of the magnetic stochasticity on electron and ion heat transport and flow damping has also been investigated in the core [45]. When plasma magnetic flux becomes stochastic, the magnetic stochasticity enhances the radial transport and the flow damping. Therefore, the PS flow should be also very small due to the profile damping (no driving force) and strong flow damping, which is consistent with the small asymmetric flows for the outward shifted R_{ax} in Figure 11. As a result, for R_{ax} of 3.75m and 3.90m, discrepancy between experimental and calculated asymmetric flows is observed even without large flow gradient.

Additionally, when the flow is compressible, the pressure on the inboard side will be higher than that on the outboard side and there should be pressure variation on a flux surface. The radial flux which is constant on a flux surface is not enough to reduce the higher pressure inboard side. In order to balance the variation of the pressure in poloidal direction, there should be strongly poloidally asymmetric radial flow. In fact, poloidal asymmetries in transport exist naturally in turbulence and collisional transport models. These effects could be considered to explain the observation on LHD. Therefore, the radial transport due to anomalous perpendicular viscosity plus strongly poloidally asymmetric radial flow other than neoclassical process could be involved in the modification of the flow structure on a flux surface in the presence of strong flow shear and outward shifted magnetic axis.

In conclusion, poloidal asymmetry of parallel flow has been observed in both NBI and ECH discharges with the application of four sets of CXS on LHD. The asymmetry of parallel flow shows a strong connection to the radial electric field. The asymmetry reverses its structure when electric field changes sign from positive to negative. Comparisons in different magnetic fields with the same magnetic configuration are made. It is found that the integrated parallel asymmetry from HFS to LFS increases linearly with the difference between the electric potential in the core and that in the edge. A model based on the incompressibility of the flow is used to explain the parallel flow asymmetry. Good agreement is found for the case with a small flow gradient, but this model fails for the case with a large flow gradient. Further, the results in various magnetic configurations show that the flow incompressibility is valid for R_{ax} = 3.55m and 3.60m when there is no external torque input. For R_{ax} = 3.75m and 3.90m, there remain some discrepancies between experiments and calculation even though external torque input is small. Poloidal variation of impurity density is also applied, while the postulated density asymmetry is opposite to the experiments. The radial transport driven by anomalous perpendicular viscosity plus strongly poloidally asymmetric radial flow could be one candidate.

Acknowledgments

The authors would like to thank the staff of LHD for their help with the experiments. This work is partly supported by the National Natural Science Foundation of China (Grant No. 11535013), JSPS KAKENHI Grant Numbers JP15H02336 and JP17H01368. This work is also partly supported by the National Institute for Fusion Science grant administrative budget NIFS10ULHH021 and NIFS17KLPH030 and by the State Scholarship Fund of CHINA SCHOLARSHIP COUNCIL.

References

[1] Groebner R. *et al* 1990 *Phys. Rev. Lett.* **64** 3015
[2] Ida K. *et al* 1990 *Phys. Rev. Lett.* **65** 1364
[3] Takechi M. *et al* 2007 *Phys. Rev. Lett.* **98** 055002
[4] Berkery J.W. *et al* 2010 *Phys. Rev. Lett.* **104** 035003
[5] Hinton F.L. and Hazeltine R.D. 1976 *Rev. Mod. Phys.* **48** 239
[6] Hirshman S.P. and Sigmar D.J. 1981 *Nucl. Fusion* **21** 1079
[7] Helander P. and Sigmar D.J. 2002 *Collisional Transport in Magnetized Plasma* (Cambridge: Cambridge University Press)
[8] Chrystal C. *et al* 2012 *Rev. Sci. Instrum.* **83**, 10D501
[9] Bortolon A. *et al* 2013 *Nucl. Fusion* **53** 023002
[10] Kumar S.T.A. *et al* 2017 *Nucl. Fusion* **57** 036030
[11] Kumar S.T.A. *et al* 2018 *Plasma Phys. Control. Fusion* **60** 054012

[12] Solomon W.M. *et al* 2006 *Phys. Plasmas* **13** 056116
[13] Tala T. *et al* 2007 *Nucl. Fusion* **47** 1012
[14] Hirsch M. *et al* 2006 *Plasma Phys. Control. Fusion* **48** S155
[15] Romé M. *et al* 2006 *Plasma Phys. Control. Fusion* **48** 353
[16] Pablant N.A. *et al* 2018 *Phys. Plasmas* **25** 022508
[17] Arévalo J. *et al* 2013 *Nucl. Fusion* **53** 023003
[18] Arévalo J. *et al* 2014 *Nucl. Fusion* **54** 013008
[19] Helander P. 1998 *Phys. Plasmas* **5** 3999
[20] Helander P. 1998 *Phys. Plasmas* **5** 1209
[21] Marr K.D. *et al* 2010 *Plasma Phys. Control. Fusion* **52** 055010
[22] Pütterich T. *et al* 2012 *Nucl. Fusion* **52** 083013
[23] Reinke M.L. *et al* 2013 *Phys. Plasmas* **20**, 056109
[24] Nishimura S. *et al* 2000 *Phys. Plasmas* **7** 437
[25] Viezzer E. *et al* 2013 *Plasma Phys. Control. Fusion* **55** 124037
[26] Yoshinuma M. *et al* 2009 *Nucl. Fusion* **49** 075036
[27] Ida K. *et al* 2010 *Nucl. Fusion* **50** 064007
[28] Nagaoka K. *et al* 2011 *Nucl. Fusion* **51** 083022
[29] Ida K. *et al* 2001 *Phys. Rev. Lett.* **86** 5297
[30] Nagaoka K. *et al* 2013 *Phys. Plasmas* **20** 056116
[31] Takeiri Y. *et al* 2010 *Fusion Sci. Technol.* **58** 482
[32] Yoshinuma M. *et al* 2010 *Fusion Sci. Technol.* **58** 375
[33] Ida K., Kado S. and Liang Y. 2000 *Rev. Sci. Instrum.* **71** 2360
[34] Sugama H. and Nishimura S. 2002 *Phys. Plasmas* **9**, 4637
[35] Boozer A.H. 1982 *Phys. Fluids* **25** 520
[36] Boozer A.H. 2005 *Rev. Mod. Phys.* **76** 1071
[37] Spong D.A. 2005, *Phys. Plasmas* **12** 056114
[38] Ida K. *et al* 2005 *Nucl. Fusion* **45** 391
[39] Hastings D.E. *et al* 1985 *Nucl. Fusion* **25** 445
[40] Yamada H. *et al* 2001 *Plasma Phys. Control. Fusion* **43** A55-A71
[41] Suzuki Y. *et al* 2016 *Nucl. Fusion* **56** 092002
[42] Ida K. *et al* 2016 *Nucl. Fusion* **56** 092001
[43] Vianello N. *et al* 2013 *Nucl. Fusion* **53** 073025
[44] Spizzo G. *et al* 2014 *Phys. Plasmas* **21**, 056102
[45] Ida K. *et al* 2015 *Nat. Commun.* **6** 5816